A HIGH-EFFICIENCY DAMPED DELTA TRIM METHOD TIGHTLY COUPLING LAGRANGIAN AND HYBRID LAGRANGIAN-EULERIAN METHODS

Yi Yuan
Politecnico di Milano
Milan, Italy

Luigi Vigevano
Politecnico di Milano
Milan, Italy

ABSTRACT

This paper introduces a novel delta trim method for helicopter rotor aerodynamics, featuring a tightly coupled mid-fidelity Lagrangian solver (DUST) and a high-fidelity hybrid Lagrangian-Eulerian solver. The primary objective is to enhance the efficiency of computationally intensive rotor trimming procedures. The method also integrates a damping factor into the Newton iteration process to accelerate convergence in both main and sub-loops of the delta scheme. Benchmark cases, including the hovering Caradonna-Tung rotor, the AH-1/OLS rotor in forward flight, and the HART II rotor in descending flight, are used to evaluate the method's performance. Results demonstrate significant reductions in computational cost, achieving over 70% CPU time savings compared to traditional methods, while maintaining comparable accuracy in predicting aerodynamic loads and control settings. The study also investigates the conditional effectiveness of the damping factor and the impact of solver initialization strategies on overall efficiency and solution fidelity.

NOTATION

*

Symbols

a Lift-curve slope

c Chord, m

C_l Lift coefficient

C_{Mx} Rolling moment coefficient

C_{My} Pitching moment coefficient

C_nM^2 Normal force coefficient

C_p Pressure coefficient

C_T Thrust coefficient

M_x Rolling moment, Nm

M_y Pitching moment, Nm

R Rotor radius, m

r^* Normalized residual

t CPU time, h

t^* Normalized CPU time, h

T Thrust, N

δ Perturbation angle, deg

ΔC_pM^2 Differential pressure coefficient

ε_M Convergence threshold for moment

ε_T Convergence threshold for thrust

λ Damping factor

λ_i Inflow ratio

μ Advance ratio

ψ Azimuth angle, deg

σ Rotor solidity

θ_0 Collective pitch angle, deg

θ_{1c} Lateral cyclic pitch angle, deg

θ_{1s} Longitudinal cyclic pitch angle, deg

*

Acronyms

BET Blade Element Theory

BL Baseline

BVI Blade-Vortex Interaction

CFD Computational Fluid Dynamics

DNW German-Dutch Wind Tunnel

FMM Fast Multipole Method

HART II Second HCC Acoustic Rotor Test

HCC Higher harmonic control

NSCBC Navier-Stokes Characteristic Boundary Condition

OLS Operational Loads Survey

RANS Reynolds-Averaged Navier–Stokes

RHS Right-Hand Side

ROSITA ROtorcraft Software ITAly

TAAT Tip Aerodynamic and Acoustics Tests

VPM Vortex Particle Method

INTRODUCTION

Numerical methods based on Eulerian (Refs. 1–3) and Lagrangian methods (Refs. 4,5) have been extensively developed and applied in the analysis of helicopter rotor aerodynamics. The Eulerian methods, such as the Reynolds-Averaged Navier-Stokes (RANS) approach, are capable of capturing the complex flow structures around rotorcrafts and their interactions with structures including rotors and wings (Refs. 6, 7). However, they often require a significant amount of computational resources, especially for high-fidelity vortex preservation involving large overset grids and multiple revolutions. On the other hand, Lagrangian methods, such as vortex particle methods, offer a more efficient alternative by representing the flow field using discrete vortices, which can be convected and diffused in a computationally efficient manner. An alternative choice, the hybrid method (Refs. 8–10) that couples the two methods, has also demonstrated its reliability and efficiency by using the Eulerian methods to predict aerodynamic loads on the rotors/wings while preserving the wake structure with Lagrangian formulation of vorticity field. Nevertheless, all three approaches require a precise control setting input as a prerequisite, usually expressed in Fourier series as

$$\theta = \theta_0 + \theta_{1c}\cos\psi + \theta_{1s}\sin\psi + \ldots \quad (1)$$

to generate not only the desired thrust and moments, but also other aerodynamic loads such as the sectional normal force. Consequently, the rotor trimming procedure is imperative, with initial values typically derived from simplified estimations or wind tunnel experiments.

Broadly, there are two categories of trim scheme in the literature: direct methods (Refs. 3, 8, 11) and delta methods (Refs. 12, 13), both of which adopt Newton's iteration procedure. The simulation of multiple rotor revolutions is required to compute the Jacobian matrix, which entries are the partial derivatives of each force and moment components with respect to each control setting. Apparently, high-fidelity Eulerian-based simulations, while capable of capturing intricate rotor wake structures and their feedback on blade loads, are computationally prohibitive – even when employed within a delta scheme. Fu et al. (Ref. 13) proposed a combination of multiple levels of grid and temporal resolutions, achieving a computational speed-up of up to 31%. Nevertheless, hundreds of thousands of CPU hours are still needed to trim the HART II case, further compounded by the complexity of generating multiple groups of overset grid systems. Ye et al. (Ref. 12) introduced a acceleration factor to the delta method, which allows for a more efficient convergence of the iterative process. However, the acceleration factor is only implemented in a hovering case, and the embedding technique was not described in detail. As a result, the trimming procedure remains a challenging and time-intensive step in rotorcraft aerodynamic analysis.

In this paper, the delta trim method is employed, together with the coupling of a mid-fidelity Lagrangian solver DUST (Ref. 4) with a high-fidelity hybrid solver (Ref. 10). The two solvers are tightly-coupled that the hybrid solver can be initialized from the latest DUST solution, inheriting all the Lagrangian elements to calculate induced velocities. A damping factor is incorporated into the delta trim method in aim of accelerating both the procedure of sub and main loop within the delta scheme. Benchmark cases are used to evaluate the accuracy of the new trimming method, and the efficiency of the method is demonstrated by comparing the computational cost with the traditional delta trim method and available literature using similar solvers (Ref. 13).

All simulations are performed on 64 cores of two AMD EPYC 7513 CPUs with speed of 2.60GHz on the high-performance cluster of Politecnico di Milano, CFDHub.

NUMERICAL METHODS

Mid-fidelity solver - DUST

The mid-fidelity solver adopted in the trim method is DUST, an open-source medium-fidelity CFD solver designed to affordably and reliably predict the interactive aerodynamics of unconventional rotorcrafts. The solver is built upon Helmholtz's decomposition of the velocity field and a Lagrangian description of incompressible vorticity field (Ref. 14). The velocity field is decomposed into a potential flow component u_ϕ and a rotational component u_ψ, which can be bound to the classical potential-based elements and the vortex particle elements respectively. The former can be modeled ranging from 1D lifting line element to 3D surface panels in need of different fidelity, while the latter is convected and diffused based on Vortex Particle Method (VPM) (Ref. 15). The computation of VPM is accelerated by a Cartesian Fast Multipole Method (FMM) (Refs. 16,17), reducing the $\mathscr{O}(N^2)$ problem to a theoretical $\mathscr{O}(N)$ problem. More detailed mathematical formulation within the solver is presented by Tugnoli (Ref. 18).

Fine-fidelity solver - hybrid solver

The high-fidelity solver is a hybrid solver that integrates the Eulerian method ROSITA (Ref. 6) and the Lagrangian method DUST developed and validated recently (Ref. 10). The RANS-based ROSITA is used to solve the near-body region covered by Eulerian structured grids, while the Lagrangian DUST is employed to preserve the wake vorticity in the grid-free farfield. The two domains are updated through an interactive scheme. From Eulerian to Lagrangian domain, the aerodynamic loads on the lifting bodies are extracted and transformed into bound vortex strength of corresponding surface elements in Lagrangian solver, following Kutta-Joukowsky theorem. From Lagrangian to Eulerian domain, the induced velocities from all the Lagrangian elements including surface elements and vortex particles correct the interface boundary of RANS grids, where Navior-Stokes Characteristic Boundary Condition (NSCBC) (Ref. 19) using ghost cells is adopted to ensure a bilateral non-reflection.

The hybrid solver allows for a more efficient computation of the rotor aerodynamics compared to a pure RANS method, as it reduces the computational resource (mainly the grid size) while maintaining a comparative accuracy of the results thanks to the Lagrangian part's ability to capture the wake vorticity.

Tightly-coupled damped delta trim algorithm

The primary concept of the trim method is to employ the Newton iteration method to solve the nonlinear relationship between the rotor aerodynamic parameters and the control settings, $(C_{T_{0,0}}, C_{Mx_{0,0}}, C_{My_{0,0}}) = F(\theta_0, \theta_{1c}, \theta_{1s})$. To efficiently compute the derivative F', or the Jacobian matrix, the delta trim method seeks to replace the high-fidelity RANS approach with a lower-fidelity yet computationally efficient method. This is achieved by introducing the so-called deltas, which bridges the two solvers and facilitates the trimming process.

Leveraging the hybrid method, which integrates both high-fidelity and mid-fidelity approaches (corresponding to RANS and the Lagrangian method, respectively), it is natural to employ the hybrid solver as the high-fidelity component and the Lagrangian solver as the mid-fidelity component in developing a new trim method. Furthermore, the hybrid solver can directly inherit the solution from the Lagrangian solver, including all body and wake elements, significantly reducing the computational cost of the traditional delta method. This is particularly beneficial in minimizing the need for high-fidelity computations, which are the most computationally expensive part in the trim procedure.

The detailed procedure of the trim method is described as follows and the flow chart is presented in Figure 1. Note that for simplicity the mid-fidelity solver is referred to as "mid solver" and the high-fidelity solver is referred to as "fine solver" in the following description.

1. Initialization of rotor control settings: the control settings could either use the experimental data directly or be estimated (Ref. 3) by

$$\begin{cases} \theta_0 = \dfrac{6C_T}{a\sigma}\left(\dfrac{1+3\mu^2/4}{1-\mu^2+9\mu^4/4}\right) - \dfrac{3}{2}\lambda_i\left(\dfrac{1-\mu^2}{1-\mu^2+9\mu^4/4}\right) \\ \theta_{1c} = 0, \theta_{1s} = 0 \end{cases} \tag{2}$$

where

$$\lambda_i = -\sqrt{\frac{\sqrt{\mu^4 + C_T^2} - \mu^2}{2}} \tag{3}$$

and a denotes lift-curve slope, σ rotor solidity, μ advance ratio and λ_i inflow ratio.

2. Initialization of mid solver: the computation is started on the mid solver to get the initial load coefficients ($C_{T_{0,0}}$, $C_{Mx_{0,0}}$, $C_{My_{0,0}}$). The first subscription denotes the index of main loop and the second is the index of sub loop. The number of revolutions depends on the flight condition. For forward flight 3-5 revolutions are needed while for hovering rotor more revolutions are expected.

3. Initialization of fine solver : the fine solver is restarted with the mid solution and a single revolution is simulated. The load coefficients are stored as (C_{T_0}, C_{Mx_0}, C_{My_0}).

4. Main loop:

   (a) Sub loop: formation of the Jacobian matrix for Newton iteration: the partial derivate of each load coefficient with respect to each control angle in the Jacobian matrix is computed by adding a small perturbation δ using the mid solver

$$\begin{cases} \dfrac{\partial C_{T_{i,j}}}{\partial \theta_0} = \dfrac{C^{\text{mid}}_{T_{i,j}}(\theta_0+\delta, \theta_{1c}, \theta_{1s}) - C^{\text{mid}}_{T_{i,j}}(\theta_0, \theta_{1c}, \theta_{1s})}{\delta} \\ \dfrac{\partial C_{Mx_{i,j}}}{\partial \theta_0} = \dfrac{C^{\text{mid}}_{Mx_{i,j}}(\theta_0+\delta, \theta_{1c}, \theta_{1s}) - C^{\text{mid}}_{Mx_{i,j}}(\theta_0, \theta_{1c}, \theta_{1s})}{\delta} \\ \dfrac{\partial C_{My_{i,j}}}{\partial \theta_0} = \dfrac{C^{\text{mid}}_{My_{i,j}}(\theta_0+\delta, \theta_{1c}, \theta_{1s}) - C^{\text{mid}}_{My_{i,j}}(\theta_0, \theta_{1c}, \theta_{1s})}{\delta} \end{cases} \tag{4}$$

$$J_{i,j} = \begin{bmatrix} \dfrac{\partial C_T}{\partial \theta_0} & \dfrac{\partial C_T}{\partial \theta_{1c}} & \dfrac{\partial C_T}{\partial \theta_{1s}} \\ \dfrac{\partial C_{Mx}}{\partial \theta_0} & \dfrac{\partial C_{Mx}}{\partial \theta_{1c}} & \dfrac{\partial C_{Mx}}{\partial \theta_{1s}} \\ \dfrac{\partial C_{My}}{\partial \theta_0} & \dfrac{\partial C_{My}}{\partial \theta_{1c}} & \dfrac{\partial C_{My}}{\partial \theta_{1s}} \end{bmatrix} \tag{5}$$

(b) Sub loop: estimation of the variations of control settings: the linear system is formulated as

$$J_{i,j}\begin{bmatrix}\Delta\theta_0\\ \Delta\theta_{1c}\\ \Delta\theta_{1s}\end{bmatrix}=RHS \tag{6}$$

where the RHS adopts the "delta trim method", linking the solutions of main loop and sub loop by

$$\begin{cases}C^{\text{delta}}_{T_{i,j}}=\Delta C_T+C^{\text{mid}}_{T_{i,j}}(\theta_0,\theta_{1c},\theta_{1s})\\ C^{\text{delta}}_{Mx_{i,j}}=\Delta C_{Mx}+C^{\text{mid}}_{Mx_{i,j}}(\theta_0,\theta_{1c},\theta_{1s})\\ C^{\text{delta}}_{My_{i,j}}=\Delta C_{My}+C^{\text{mid}}_{My_{i,j}}(\theta_0,\theta_{1c},\theta_{1s})\end{cases} \tag{7}$$

where

$$\begin{cases}\Delta C_T=C^{\text{fine}}_{T_{i-1}}(\theta_0,\theta_{1c},\theta_{1s})-C^{\text{mid}}_{T_{i,0}}(\theta_0,\theta_{1c},\theta_{1s})\\ \Delta C_{Mx}=C^{\text{fine}}_{Mx_{i-1}}(\theta_0,\theta_{1c},\theta_{1s})-C^{\text{mid}}_{Mx_{i,0}}(\theta_0,\theta_{1c},\theta_{1s})\\ \Delta C_{My}=C^{\text{fine}}_{My_{i-1}}(\theta_0,\theta_{1c},\theta_{1s})-C^{\text{mid}}_{My_{y_{i,0}}}(\theta_0,\theta_{1c},\theta_{1s})\end{cases} \tag{8}$$

and the RHS is expressed as

$$RHS=\begin{bmatrix}C^{\text{target}}_{T}-C^{\text{delta}}_{T_{i,j}}\\ C^{\text{target}}_{Mx}-C^{\text{delta}}_{Mx_{i,j}}\\ C^{\text{target}}_{My}-C^{\text{delta}}_{My_{i,j}}\end{bmatrix} \tag{9}$$

(c) Sub loop : update of the control settings: a damping factor λ is used to accelerate the convergence. In this step, an extra check of the variations of control settings is applied, if they are less than a small quantity ε_θ, the sub loop exits.

$$\begin{bmatrix}\theta_0^{\text{new}}\\ \theta_{1c}^{\text{new}}\\ \theta_{1s}^{\text{new}}\end{bmatrix}=\lambda\begin{bmatrix}\Delta\theta_0\\ \Delta\theta_{1c}\\ \Delta\theta_{1s}\end{bmatrix}+\begin{bmatrix}\theta_0\\ \theta_{1c}\\ \theta_{1s}\end{bmatrix} \tag{10}$$

(d) Sub loop: verification: the updated control settings are verified with mid solver. The sub loop exits if the load coefficients $(C_{T_{i,j+1}}, C_{Mx_{i,j+1}}, C_{My_{i,j+1}})$ meet the convergence criterion, otherwise the procedure goes back to step 4a. The original determination formula is written as Equation 11.

$$\begin{cases}\left|C^{\text{delta}}_{T_{i,j+1}}-C^{\text{target}}_{T}\right| \le \varepsilon_T\cdot C^{\text{target}}_{T}\\ \left|C^{\text{delta}}_{Mx_{i,j+1}}-C^{\text{target}}_{M_x}\right| \le \varepsilon_M\cdot C^{\text{target}}_{Mx}\\ \left|C^{\text{delta}}_{My_{i,j+1}}-C^{\text{target}}_{M_y}\right| \le \varepsilon_M\cdot C^{\text{target}}_{My}\end{cases} \tag{11}$$

However, with the incorporation of the damping factor λ, three strategies can be employed to improve the convergence behavior of the iterative process:

i. Damping applied only in sub loops: The original update formula is adopted, and the damping factor λ is applied solely within the sub loop iterations. As a result, the main loop updates are unaffected because $\Delta C_{T/M}$ remains constant throughout a single main loop.

ii. Damping applied only in the main loop verification step: The damping is introduced only when updating the control settings in the main loop, using the expression $\theta^{\text{new}}=\lambda\Delta\theta+\theta$. Sub loop iterations remain unchanged. However, this approach requires the mid-level solver to recompute the initial load coefficients in each new main loop instead of reusing the final values from the last iteration, adding one extra revolution of mid solver computation per main loop.

iii. Simultaneous damping in both sub and main loops: the original determination formula can be recasted after substituting Equation 7 and 8 as

$$\begin{aligned}C^{\text{mid}}_{T/M_{i,j+1}}(\theta+\Delta\theta)+C^{\text{fine}}_{T/M_{i-1}}(\theta)\\ -C^{\text{mid}}_{T/M_{i,0}}(\theta)-C^{\text{target}}_{T/M}\\ =\varepsilon\end{aligned} \tag{12}$$

Assuming a linear relationship of $C^{\text{mid}}_{T/M}$ and control settings over the range of $[\theta,\theta+\Delta\theta]$ inspired by the formation of Jacobian matrix in Newton iteration, the following equation holds.

$$\begin{aligned}C^{\text{mid}}_{T/M_{i,j+1}}(\theta+\lambda\Delta\theta)-C^{\text{mid}}_{T/M_{i,0}}(\theta)\\ =\lambda(C^{\text{target}}_{T/M}-C^{\text{fine}}_{T/M_{i-1}}(\theta))+\varepsilon\end{aligned} \tag{13}$$

This leads to a damped convergence criterion that accounts for the effect of damping factor λ:

$$\begin{aligned}|C^{\text{mid}}_{T/M_{i,j+1}}(\theta+\lambda\Delta\theta)-C^{\text{mid}}_{T/M_{i,0}}(\theta)\\ -\lambda(C^{\text{target}}_{T/M}-C^{\text{fine}}_{T/M_{i-1}}(\theta))|\\ <\varepsilon_{T/M}\cdot C^{\text{target}}_{T/M}\end{aligned} \tag{14}$$

where the deltas in Equation 8 become $(\lambda C^{\text{fine}}_{T/M_{i-1}}-C^{\text{mid}}_{T/M_{i,0}})$ and the target coefficient $\lambda C^{\text{target}}_{T/M}$. The damped convergence criterion naturally degenerates to the original convergence criterion when $\lambda=1.0$ and a more controlled and robust iteration convergence is expected with an appropriate value of λ.

5. Main loop: verification: the updated control settings are verified again by fine solver which is initialized from either the latest mid solver or fine solver solution. The trim procedure is finished if the original criterion (Equation 11) is met (substitute $C^{\text{delta}}_{T_{i,j+1}}$ with $C^{\text{fine}}_{T_i}$), otherwise another main loop is required again from Step 4a.

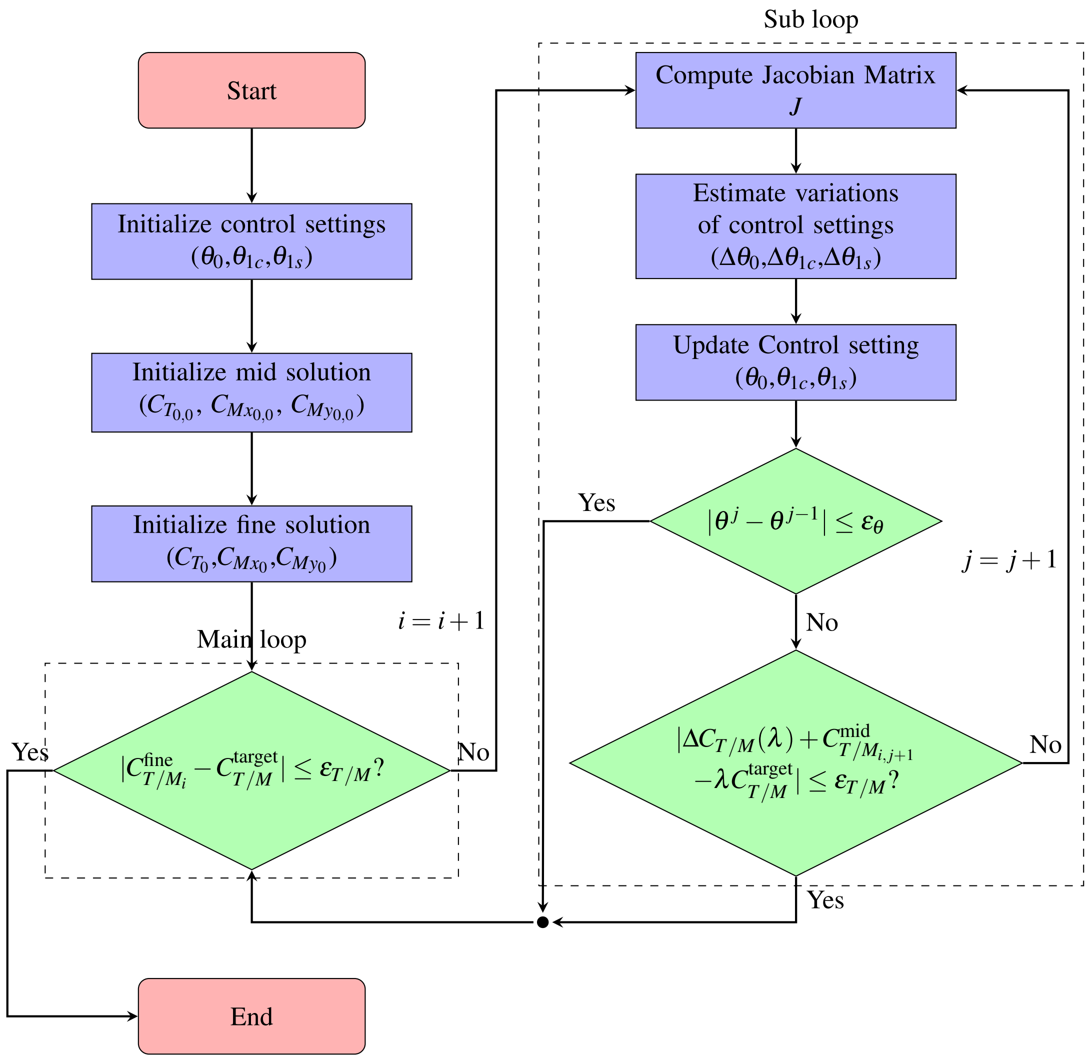

Figure 1: Flow chart of the delta trim method

Variants of the method

The modularity of the proposed methodology allows to test different variants of the method itself. In Step 3, when initializing the fine solution, the fine solver can be either restarted from mid solution of Step 2 to accelerate the trimming process, or conducted independently from itself. In Step 5, when verifying the convergence, the fine solver can also be either restarted from the latest mid solution, or from the latest fine solution without accuracy losses. The combinations of these two steps lead to three different coupling conditions of trimming, which are summarized in Table 1.

Table 1: Verification matrix

Label	source of Step 3	source of Step 5
Hybrid	fine solution	fine solution
DUST	mid solution	mid solution
DUST init	mid solution	fine solution

The first condition, Hybrid, is the classical delta trim method without ”tightly-coupling” and is used as a baseline case for the new trim method. The second and third conditions, DUST and DUST init, are the presented trim method with full coupling and partial coupling respectively. In the following discussion, the damping factor is added to the end of the label name in case the iteration is damped.

RESULTS AND DISCUSSION

Caradonna-Tung rotor

The hovering Caradonna-Tung rotor is used as a preliminary validation of the proposed delta-trim method. Since the rotor is quasi-steady and only the collective pitch and thrust coefficient C_T are considered, the trim procedure is significantly simplified such that the Jacobian matrix is degraded into a scalar form, retaining only the $\partial C_T / \partial \theta_0$ component. The simulation setup including the operation condition, Eulerian grids, Lagrangian modelling is described in the previous work (Ref. 10). The mid solver is initialized with 10 rotor revolutions, and the Hybrid and DUST variants are used. The convergence criterion ε_T is set to 1×10^{-2} and the damping factor λ is set to 1.0 to initially study the convergence character of the trim procedure.

Figure 2 shows the trimming convergence history under current setup, and the target C_T is given with an error strip in Figure 2b. Both methods meet the convergence criterion after three loops with similar convergence pattern. The values of collective pitch and thrust coefficient of the two variants differ slightly as listed in Table 2, assessing the accuracy of the tight-coupling strategy.

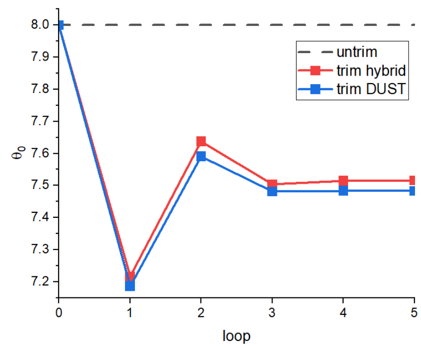

(a) θ_0

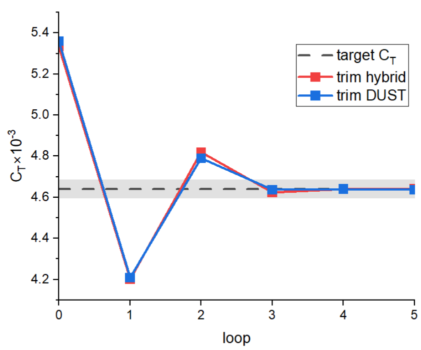

(b) C_T

Figure 2: Rotor Caradonna-Tung: trimming convergence history using different methods

Table 2: Rotor Caradonna-Tung: trimmed control settings using different methods compared with experiment (r^*: normalized residual)

Method	θ_0	$C_T \times 10^{-3}$	$r^* \times 10^3$
Exp	8.0	4.64	-
Hybrid	7.50	4.62	-3.7
DUST	7.48	4.64	-0.7

The spanwise lift coefficient and sectional pressure distributions of the rotor obtained using the untrimmed and the two trimmed solutions are compared in Figure 3, against experimental data. Overall, both trimming methods improve the agreement with experiment, implying virtually the same accuracy. While the spanwise lift coefficient does not exactly match the experimental values, it retains the same trend as the untrimmed case, probably due to numerical limitations inherent to the hybrid solver.

In Step 4c and Step 4d, a damping factor λ is introduced into the trim procedure to accelerate convergence. As shown in Figure 4, setting $\lambda = 1.0$ - equivalent to the original delta trim method - leads to oscillatory convergence, with overshooting before stabilizing after three main loops. A threshold value of $\lambda = 0.6$ enables convergence within a single main loop, while larger values cause overshooting and smaller values result in undershooting. When λ is further reduced (e.g., to 0.4 or below in this case), convergence deteriorates due to inconsistencies in the thrust predicted by DUST under hovering condition unless a larger tolerance is adopted ($\varepsilon_T' = 1.5\varepsilon_T$).

The influence of the damping factor on the number of main and sub loops, and the corresponding elapsed CPU time is reported in Table 3. Note that the convergence criterion in the $\lambda = 0.4$ case is manually calibrated ($\varepsilon_T' = 1.5\varepsilon_T$), and the $\lambda = 1.0$ case, corresponding to the original method, is serving as the baseline for comparison. By reducing the number of loops, the $\lambda = 0.8$ and 0.6 cases significantly improve the efficiency, with the normalized CPU time dropping to 0.70 and 0.44, respectively. However, further reduction of λ leads to an increase in both loops and CPU time. This trend confirms that a properly selected damping factor can considerably enhance convergence and computational performance. Specifically, in this overshooting-prone case, a damping factor slightly below 1.0 proves preferable.

Table 3: Rotor Caradonna-Tung: acceleration effect of the damping factor (t^*: normalized CPU time)

λ	Main loop	Sub loop	t^*
1.0	3	6	1.0
0.8	2	5	0.70
0.6	1	2	0.44
0.5	2	4	0.69
0.4	3	5	0.89

The comparison of CPU time costs for the two trim methods with $\lambda = 1.0$ is presented in Table 4. When the fine solver initialization is performed using the hybrid solver itself (denoted as hybrid in the table), approximately 89.1% of the total CPU time is consumed during this initialization stage, due to the requirement of simulating 10 rotor revolutions under hovering conditions. By contrast, if the initialization is based on the mid solver (DUST) solution, the total time is dramatically reduced to 15% of the hybrid case. This clearly demonstrates that initializing from the mid solver significantly enhances computational efficiency.

AH-1/OLS rotor in forward flight

The second validation case is the 1/7-scale model of the AH-1 helicopter main rotor, referred to as the AH-1/OLS ro-

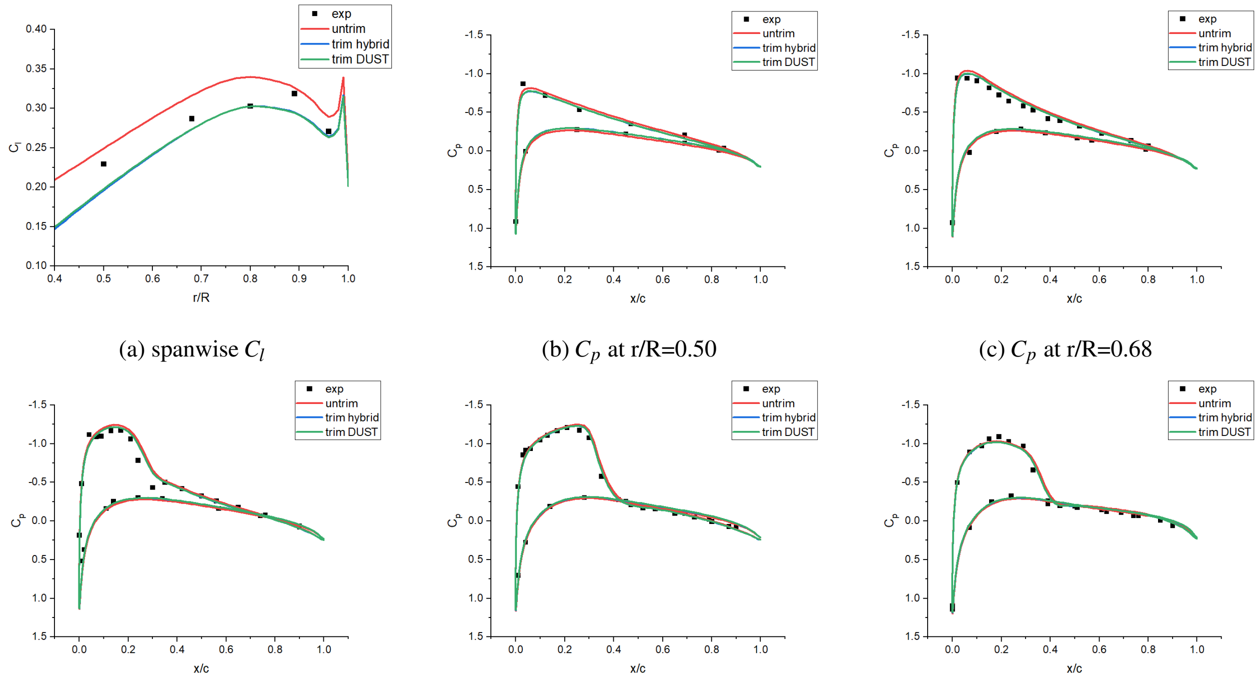

(a) spanwise C_l (b) C_p at r/R=0.50 (c) C_p at r/R=0.68

(d) C_p at r/R=0.80 (e) C_p at r/R=0.89 (f) C_p at r/R=0.96

Figure 3: Rotor Caradonna-Tung: trimmed spanwise lift coefficient and sectional pressure distributions using different methods compared with experiment

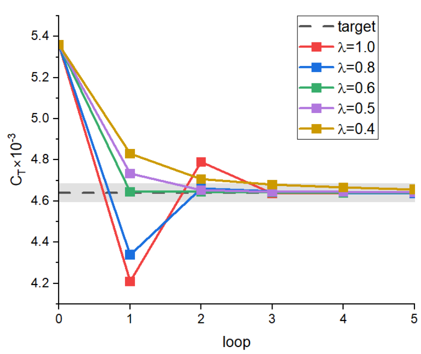

Figure 4: Rotor Caradonna-Tung: trimming convergence history with different damping factor

tor, which was tested in the German-Dutch Wind Tunnel (DNW) (Ref. 20). The rotor comprises two rectangular blades with a radius of 0.958m and a chord of 0.1039m. The blades are linearly twisted by $-10°/R$ from root to tip, starting at a root-cut at 0.182R, and employ the OLS/TAAT airfoil. The

Table 4: Rotor Caradonna-Tung: CPU time cost using different trim methods (t: CPU time, t_{init}: initialization CPU time of fine solver, t^*: normalized CPU time)

Method	Main loop	Sub loop	t(h)	t_{init}(h)	t^*
Hybrid	3	6	500	440	1.0
DUST	3	6	73	14	0.15

operating condition selected is test case 10014 (Ref. 21), which represents a typical low-speed descending flight where blade-vortex interaction (BVI) effects are pronounced. The tip Mach number is 0.664 and the advance ratio is 0.164. The rotor shaft angle is set to 0°, while the tip-path plane angle α_{TPP} is tilted backward by 1° via adjustment of the longitudinal flapping. The initial blade control settings are

$$\begin{cases} \theta(\psi) = 6.14 + 0.9\cos\psi - 1.39\sin\psi \\ \beta(\psi) = 0.5 - 1.0\cos\psi \end{cases} \tag{15}$$

resulting in a target thrust coefficient of 0.0054, and zero moment loads.

The dimension of the body-fitted blade grid needed in the hybrid solver is $233 \times 93 \times 43$ with 2.13M nodes in total, extending 1.0c outwards from the blade surface in all direction. The first layer thickness is set to $4 \times 10^{-5}c$ to keep $y+ \approx 1$. The maximum grid spacing constrained to approximately $0.1c$. The rotor blades are modeled using 50 uniformly distributed lifting line elements. Each revolution is discretized into 72 physical time steps.

In the initialization step of the trim procedure, the rotor performs 5 revolutions in the mid solver. Two approaches for initializing the fine solver are tested respectively: one using the hybrid solver itself, and the other using the DUST solution. In Step 5, the fine solver is restarted from both the hybrid and DUST solutions to assess their impact. The convergence criteria are set to $\varepsilon_T = 1 \times 10^{-2}$ and $\varepsilon_M = 1 \times 10^{-5}$, and in the sub loop ε_M is set to 1×10^{-4}.

Figure 5 presents the trimming convergence history of control settings and aerodynamic loads, where a damping factor of 0.8 is adopted in the last case. All configurations show satisfactory convergence behavior and meet the specified convergence criterion within three main loops, with shaded error bands indicating confidence region. Among the parameters, the convergence of the pitch moment coefficient C_{M_y} appears relatively noisy. However, when taking the "hybrid" configuration as the baseline, the "DUST" configuration shows significant discrepancies in the converged values. In contrast, both "DUST init" and "DUST init $\lambda = 0.8$" produce results that closely align with the baseline, indicating higher accuracy. Moreover, the inclusion of a damping factor contributes to a smoother convergence process for θ_0, θ_{1c} and C_T, yet it does not reduce the number of main loops.

To quantitatively evaluate the trimmed results, Table 5 summarizes the trimmed control settings, the corresponding thrust coefficient, and the residuals after three main loops. It should be noted that the differences in control settings between Fu's and the "hybrid" results arise from inherent distinctions between the ROSITA and hybrid solvers. The descrepencies in trimmed control settings between the baseline "hybrid" solution and those of "DUST init" and "DUST init $\lambda = 0.8$" are all within 0.1°. Among them, the "DUST init $\lambda = 0.8$" configuration exhibits overall smaller residuals compared to "DUST init".

A deeper insight in the significant discrepancies between the "hybrid" and "DUST" configurations can be deduced from the disk plane loads, as is presented in Figure 6. The contour in Figure 6(a) is the azimuth derivative of C_nM^2 of the final revolution of the hybrid initialization (baseline) and Figure 6(b) and (c) illustrate the corresponding quantities from the "DUST" configuration during the initialization stage for two blades, where black markers denote BVI with vortices generated during the current revolution, while red markers represent BVI with older vortices predicted by the DUST solver. Among the two blades, the loading on blade 1 shows the closer agreement with the baseline solution. In contrast, blade 2 shows substantial deviations from the baseline. Notably, in region A marked with red circles, blade 2 exhibits no significant drop in C_nM^2, indicating that the wake predicted by DUST in this region is weak. Similarly, the BVI event in region D is barely captured. Moreover, regions B, C, and D exhibit exaggerated load variations near the blade root, significantly compromises simulation fidelity. The phenomena indicate that the DUST configuration is suboptimal unless its wake predictions can be enhanced to match the fidelity of those produced by the hybrid solver.

In the settings of previous results, the sub loop uses looser convergence criteria thanthe main loop, and the damping factor have little effect on acceleration. Further investigation shows that applying stricter criteria - equal to those of the main loop - improves efficiency. Table 6 summarizes the control settings, loop counts, and normalized CPU times using different criteria and damping factors. The fourth case applies the damping factor only to the collective pitch θ_0, indicated by the subscript "0". While control angles remain nearly identical, stricter criteria increase sub-loop iterations. Nonetheless, applying damping under strict conditions reduces CPU time to 0.815 by eliminating one main loop.

Figure 7 presents the trimmed sectional pressure distributions at r/R=0.955 across five azimuthal angles ($\psi = 0^\circ$, 45°, 90°, 135°, 180°), comparing computational results with experimental data. The "DUST" solution is omitted. At all azimuth positions, the three trimmed solutions are basically overlapped and provide more reasonable agreement with experimental measurements, particularly in the leading-edge peak region against the untrimmed pressure distribution. A similar trend is observed in Figure 8, which depicts the differential pressure ΔC_pM^2 near the leading edge at $x/c = 0.03$ as a function of azimuth angle. The improvements are most notable between the two pressure peaks, from approximately 80° to 290° although the overprediction remains, consistent with Yu's observations (Ref. 21). These comparisons highlight the effectiveness of the proposed trim method in producing more accurate and physically realistic pressure distributions.

The efficiency of the present trim method is compared with Fu's dual-dimensional approach (Ref. 13) in Table 7. Due to differences in CPU configurations, number of physical time steps per revolution, and grid sizes between the two studies, a direct comparison is not straightforward. To account for hardware differences, a CPU performance correction factor based on the PassMark benchmark (Ref. 22) is applied. The body-fitted grid sizes are also considered. However, variations in time step resolution and mesh size of background grids are not normalized, as these are inherent to the respective solver implementations and not isolated. Compared to Fu's method, the proposed trim approach reduces the CPU time by 79%. Furthermore, when initialized with the DUST solution, the CPU time is reduced by an additional 42.7%, owing to the tightly-coupled Lagrangian system between the hybrid and DUST solvers.

HART II rotor in descending flight

The HART II rotor, a 40% Mach-scaled model of the BO-105 four-bladed hingeless rotor tested in DNW (Ref. 23), is severed as the third case. Each of the rectangular blades has a radius of 2.0m, a chord of 0.121 m, and a linear twist of $-8^\circ/R$. The blades adopt a modified NACA 23012 airfoil with a trailing-edge tab. The rotor has a precone of 2.5°. The selected operation condition, the baseline (BL) condition, corresponds to a descending flight with an effective shaft angle of 4.5°, an advance ratio of 0.15, a tip Mach number of 0.64. The blades are assumed to be rigid, ensure the consistency of initial condition (Ref. 13). The blade kinematics are imposed directly from experimental data as

$$\theta(\psi) = 3.8 + 1.92\cos\psi - 1.34\sin\psi \tag{16}$$

The target thrust is $3300N$, and the roll and pitch moments are $20N \cdot m$ and $-20N \cdot m$ respectively.

The Eulerian blade grid has a resolution of $205 \times 114 \times 39$, resulting in approximately 1.92 million nodes. The first layer

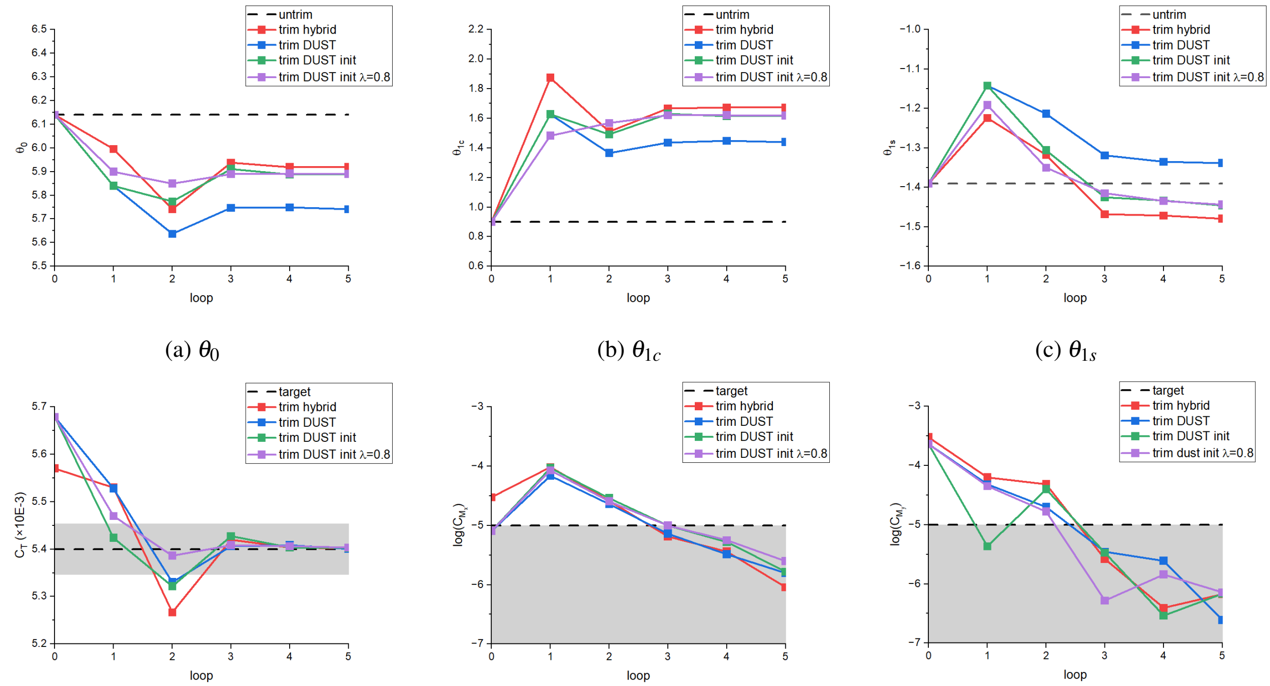

(a) θ_0 (b) θ_{1c} (c) θ_{1s}

(d) C_T (e) C_{M_x} (f) C_{M_y}

Figure 5: Rotor AH-1/OLS: trimming convergence history using different methods

Table 5: Rotor AH-1/OLS: trimmed control settings using different trim methods compared with experiment (r_T^*: normalized thrust residual, r_M^*: moment residual)

Method	θ_0	θ_{1c}	θ_{1s}	$C_T \times 10^{-3}$	$r_T^* \times 10^3$	$\log\lvert r_{M_x}\rvert$	$\log\lvert r_y\rvert$
Exp	6.14	0.9	-1.39	5.4	-	-	-
Fu (Ref. 13)	5.72	1.63	-1.40	5.40	0.0	-5.8	-5.2
Hybrid	5.92	1.67	-1.47	5.42	3.7	-5.2	-5.6
DUST	5.75	1.44	-1.32	5.41	1.9	-5.1	-5.5
DUST init	5.91	1.63	-1.43	5.43	5.1	-5.0	-5.5
DUST init $\lambda = 0.8$	5.89	1.62	-1.41	5.41	1.6	-5.0	-6.3

thickness is set to $5 \times 10^{-5}c$, and the global maximum grid spacing is limited to $0.15c$, following the standard setting of Reference (Ref. 24). For the Lagrangian computations in both the hybrid and DUST solvers, each blade is discretized into 50 uniformly lifting line elements, with 90 physical time steps per revolution. A particle overlapping ratio of 1.3 is employed.

The rotor is initialized in the mid solver for 3 revolutions. Subsequently, the fine solver is initialized either from its own or from the DUST result. However, because the DUST solution deviates significantly from both the experimental data and the hybrid solver results, the hybrid solver uses its own Lagrangian solution in the iteration process to prevent the propagation of errors, as indicated in the prior test case. The convergence criteria is set to $\varepsilon_T = \varepsilon_M = 1 \times 10^{-2}$ and for looser sub loops $\varepsilon_M = 0.5$.

The trimming convergence history is presented in Figure 9. The same setup of applying the damping factor only on collective pitch is tested. It can be observed that the thrust converges most rapidly, meeting the convergence criterion after only two main loops. In contrast, the moment converges more slowly. Under looser convergence criteria(indicated by the lighter error stripe), the moment satisfies the sub-loop criterion after three main loops, except the ”DUST init $\lambda_0 = 0.8$” configuration, and the main-loop criterion is met after five main loops for all the cases, suggesting that the effectiveness of the damping factor is conditionally influenced by the nonlinear relationship between control settings and aerodynamic loads.

The trimmed control settings and aerodynamic loads after five main loops are summarized in Table 8, with the corresponding residuals listed in Table 9. The results reported in Reference (Ref. 13) do not achieve the same level of accuracy as those obtained in the present study. Unlike the rotor AH-1/OLS case, where differences in control settings are more pronounced, the variations among different setups are negligible when using the ”hybrid” configuration as the baseline. This confirms the effectiveness of the tightly-coupled strategy

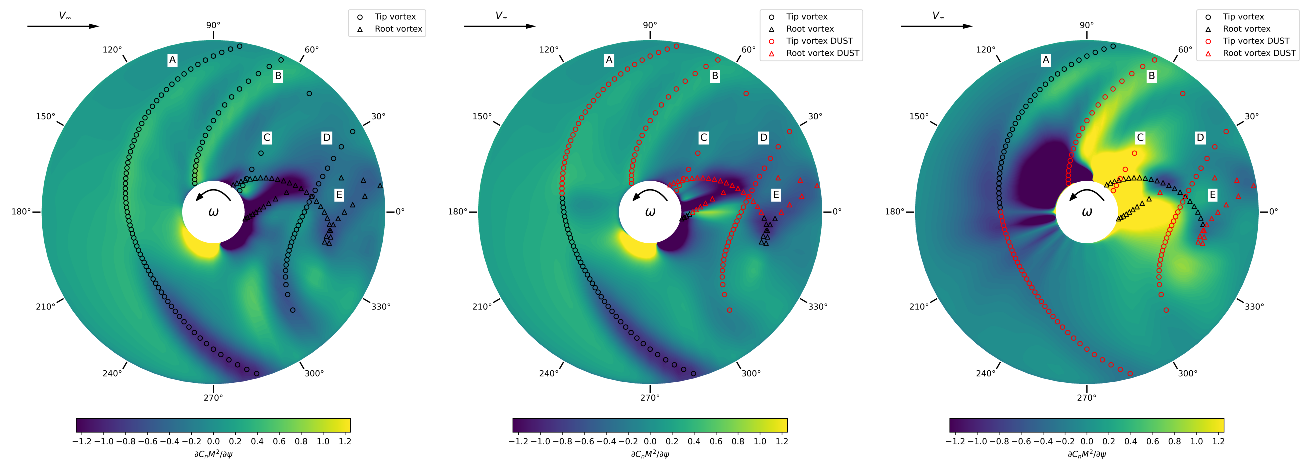

(a) trim hybrid(baseline)

(b) trim DUST init blade 1

(c) trim DUST init blade 2

Figure 6: Rotor AH1-OLS: the azimuthal derivative of the normal force coefficient on the rotor disk initialized by DUST compared with hybrid solution

Table 6: Rotor AH-1/OLS: trimming results and CPU time using different convergence criteria and damping factors(t^*: normalized CPU time)

Method	θ_0	θ_{1c}	θ_{1s}	Main loop	Sub loop	t^*
loose $\lambda = 1.0$	5.91	1.63	-1.43	3	4	1.00
loose $\lambda = 0.8$	5.89	1.62	-1.41	3	4	0.99
strict $\lambda = 1.0$	5.89	1.63	-1.46	3	7	1.08
strict $\lambda_0 = 0.8$	5.89	1.65	-1.42	2	5	0.82

Table 7: Rotor AH-1/OLS: CPU time cost using different trim methods (t: CPU time, t^*_{corr}: corrected normalized CPU time)

method	main loop	t(h)	t^*_{corr}
Fu (Ref. 13)	6	9758	1.0
Hybrid	3	1228	0.21
DUST init	3	704	0.11

between the two solvers applied at the initialization stage.

Figure 10 shows the trimmed sectional normal force C_nM^2 at r/R=0.87 by different configurations with respect to the untrimmed one and experiment data by conditional averaging (Ref. 25). The untrimmed solution markedly overpredicts the loading across the entire azimuth range. After applying the trimming procedure, both the "hybrid" and "DUST init" configurations show substantial improvement in capturing the overall shape and magnitude of the C_nM^2 distribution when compared with experimental data. Nevertheless, the averaged C_nM^2 remains overpredicted by 16.2%, and the simulations fail to reproduce the characteristic oscillatory behavior induced by BVI in the azimuthal sectors of [0°, 110°] and [260°, 360°]. This discrepancy can be attributed to coarse temporal and spatial resolution, and more critically, to the omission of blade elasticity effects.

The CPU time costs of different methods are corrected based on the aforementioned estimation and summarized in Table 10. The number of main loops shown here is chosen by guaranteeing the same degree of residuals as that in Fu's work.The proposed DUST-hybrid delta trim approach achieves a 76.1% reduction in computational time compared to the BET-ROSITA method, with an additional 18.8% savings attainable through tight-coupling of the two solvers.

CONCLUSIONS

This paper develops a novel delta trim method featured with a tightly-coupling of the mid- and high-fidelity solver as well as a damped Newton iteration connecting the main and sub loops. Main conclusions are as follows:

1. Employing the hybrid solver as the fine solver benefits the trim algorithm not only from the high efficiency of the approach, but also from a tight coupling with the mid-level solver. The first advantage leads to a CPU time saving of over 70%. The second avoids simulating several rotor revolutions at initialization stage, offering notable efficiency gains at the same time.

2. The acceleration effect of a damping factor is conditionally relevant to the complexity of the control settings and aerodynamic loads, and its optimal value is often empirically determined. In general, there exists an ideal value that yields the best performance and a value close to 1 is typically a safe and robust choice.

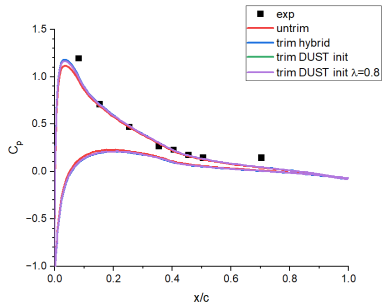

(a) $\psi = 0°$

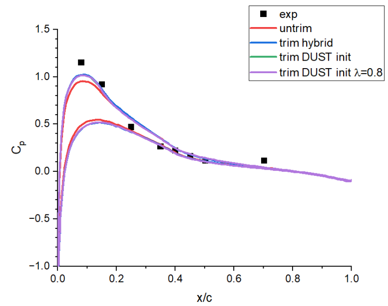

(b) $\psi = 45°$

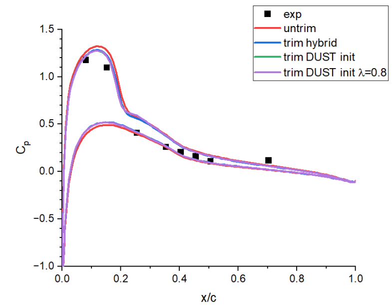

(c) $\psi = 90°$

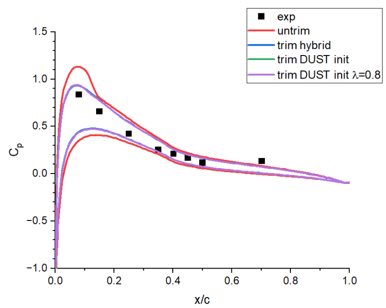

(d) $\psi = 135°$

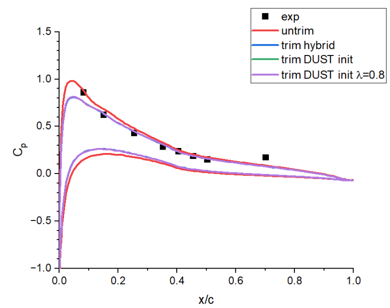

(e) $\psi = 180°$

Figure 7: Rotor AH-1/OLS: trimmed sectional pressure distributions at $r/R = 0.955$ and several azimuth positions using different methods compared with experiment

Table 8: Rotor HART II: trimmed control settings and aerodynamic loads using different trim methods compared with experiment

Method	θ_0	θ_{1c}	θ_{1s}	$T(N)$	$M_x(N)$	$M_y(N)$
Exp	3.80	1.92	-1.34	3300	20	-20
Fu (Ref. 13)	2.24	2.03	-1.28	3315.6	26.8	-21.5
Hybrid	2.24	2.23	-1.26	3299.9	20.1	-20.0
DUST init	2.24	2.23	-1.25	3300.0	20.1	-20.1
DUST init $\lambda_0 = 0.8$	2.24	2.23	-1.25	3300.1	20.1	-20.0

Table 9: Rotor HART II: trimmed residuals using different trim methods compared with experiment (r_T^*: normalized thrust residual, r_M^*: normalized moment residual)

Method	$r_T^* \times 10^3$	$r_{M_x}^* \times 10^2$	$r_{M_y}^* \times 10^2$
Fu (Ref. 13)	4.7	34.0	-7.5
Hybrid	-0.03	0.37	-0.04
DUST init	0.02	0.67	-0.40
DUST init $\lambda_0 = 0.8$	0.02	0.56	-0.21

Table 10: Rotor HART II: CPU time cost using different trim methods (t: CPU time, t^*_{corr}: corrected normalized CPU time)

method	main loop	t(h)	t^*_{corr}
Fu (Ref. 13)	9	14305	1.0
Hybrid	3	3456	0.24
DUST init	3	2807	0.20

3. The accuracy of the presented delta trim method primarily depends on the fidelity of the hybrid (fine) solver. Although the tight coupling slightly affect the results, the impact remains acceptable given the tolerance. The fine solver can be restarted from mid solution at verification stage only when the latter provides correct wake.

Author contact: Yi Yuan yi.yuan@polimi.it Luigi Vigevano luigi.vigevano@polimi.it

ACKNOWLEDGMENTS

The authors acknowledge the computational resource of the high performance cluster CFD-Hub at Politecnico di Milano. The author Yi Yuan would like to thank the China Scholarship Council for financial support under the Grant No. 202006250025.

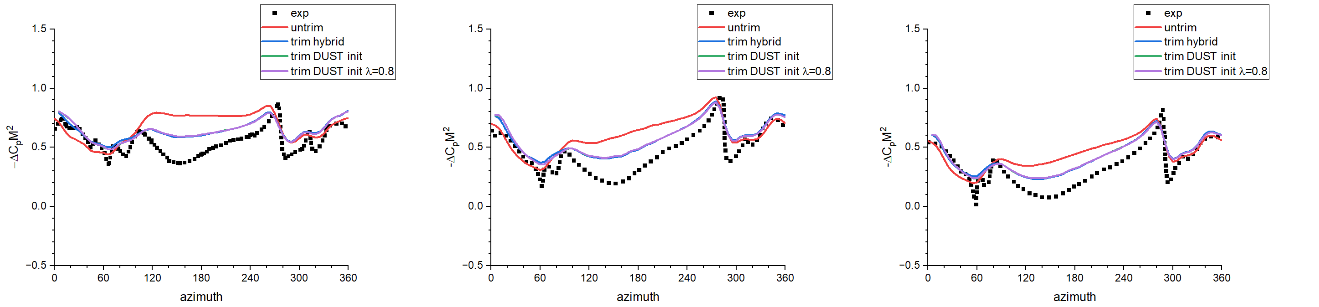

(a) $r/R = 0.8$ (b) $r/R = 0.91$ (c) $r/R = 0.975$

Figure 8: Rotor AH-1/OLS: untrimmed and trimmed differential pressure near the leading edge ($x/c = 0.03$) using different methods compared with experiment

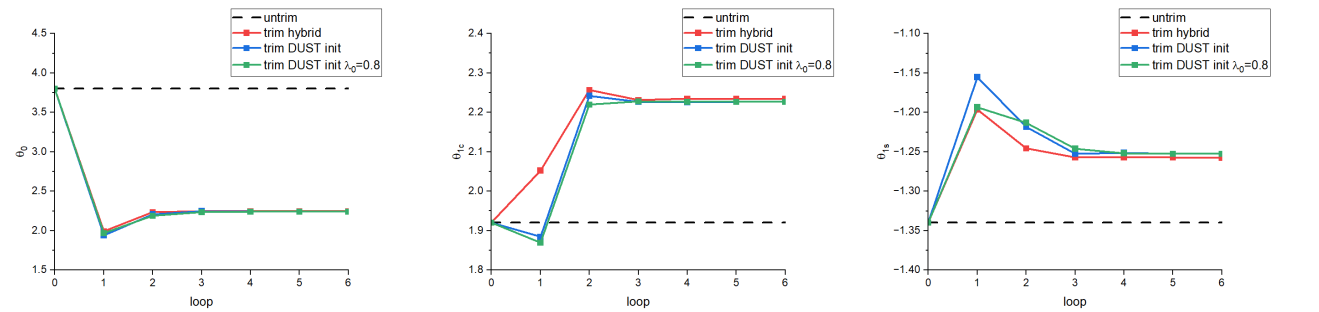

(a) θ_0 (b) θ_{1c} (c) θ_{1s}

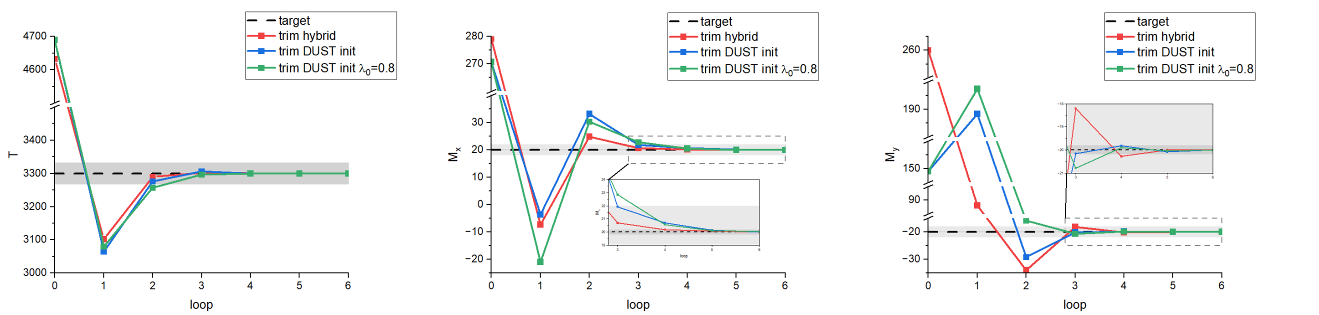

(d) T (e) M_x (f) M_y

Figure 9: Rotor HART II: trimming convergence history using different methods

REFERENCES

1. Abras, J. N., and Hariharan, N., "Comparison of Computational Fluid Dynamics Hover Predictions on the S-76 Rotor," *Journal of Aircraft*, Vol. 55, (1), January 2018, pp. 12–22. DOI: 10.2514/1.C034121.

2. Fu, J., Yuan, Y., and Vigevano, L., "Assessment of the Vortex Feature-Based Vorticity Confinement Method Applied to Rotor Aerodynamics and Aeroacoustics," *Aerospace*, Vol. 10, (5), May 2023, pp. 447. DOI: 10.3390/aerospace10050447.

3. Steijl, R., Barakos, G., and Badcock, K., "A Framework for CFD Analysis of Helicopter Rotors in Hover and Forward Flight," *International Journal for Numerical Methods in Fluids*, Vol. 51, (8), July 2006, pp. 819–847. DOI: 10.1002/fld.1086.

4. Niro, C., Savino, A., Cocco, A., and Zanotti, A., "Mid-Fidelity Numerical Approach for the Investigation of Wing-Propeller Aerodynamic Interaction," *Aerospace Science and Technology*, Vol. 146, March 2024, pp. 108950. DOI: 10.1016/j.ast.2024.108950.

5. Alvarez, E. J., and Ning, A., "Modeling Multirotor Aerodynamic Interactions Through the Vortex Particle Method," AIAA Aviation 2019 Forum, June 2019. DOI: 10.2514/6.2019-2827.

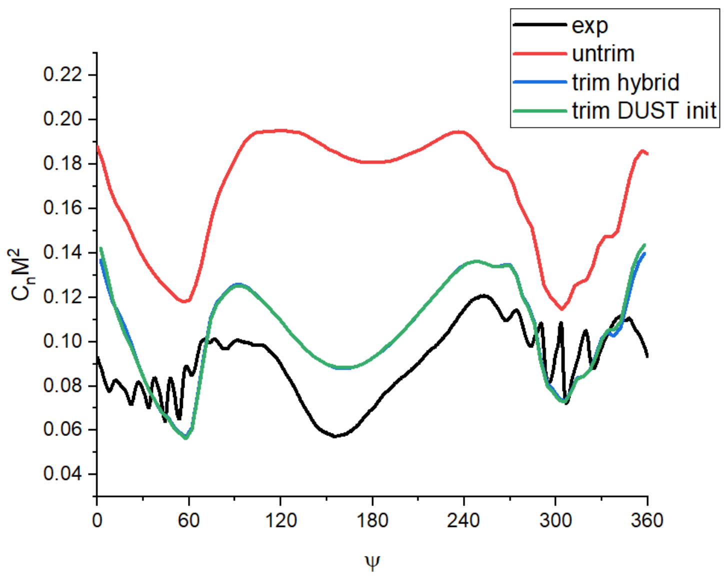

Figure 10: Rotor HART II: untrimmed and trimmed normal force coefficient at $r/R = 0.87$ using different methods compared with experiment

6. Biava, M., and Vigevano, L., "Simulation of a Complete Helicopter: A CFD Approach to the Study of Interference Effects," *Aerospace Science and Technology*, Vol. 19, (1), June 2012, pp. 37–49. DOI: 10.1016/j.ast.2011.08.006.

7. Zhang, T., Barakos, G. N., Furqan, and Foster, M., "High-Fidelity Aerodynamic and Acoustic Design and Analysis of a Heavy-Lift eVTOL," *Aerospace Science and Technology*, Vol. 137, June 2023, pp. 108307. DOI: 10.1016/j.ast.2023.108307.

8. Wang, L., Xu, G., and Shi, Y., "Development and Validation of a Hybrid Method for Predicting Helicopter Rotor Impulsive Noise," *Proceedings of the Institution of Mechanical Engineers, Part G: Journal of Aerospace Engineering*, Vol. 233, (4), March 2019, pp. 1323–1339. DOI: 10.1177/0954410018756476.

9. Moushegian, A. M., and Smith, M. J., "Dual-Solver Hybrid Computational Approach to Integrated Propulsion Aerodynamics," *Journal of Aircraft*, Vol. 60, (2), 2023, pp. 521–532. DOI: 10.2514/1.C036808.

10. Yuan, Y., and Vigevano, L., "Assessment of a Hybrid Eulerian-Lagrangian Method by Comparison with Its Parent Codes," 50th European Rotorcraft Forum (ERF 2024), 2024.

11. Yang, Z., Sankar, L. N., Smith, M. J., and Bauchau, O., "Recent Improvements to a Hybrid Method for Rotors in Forward Flight," *Journal of Aircraft*, Vol. 39, (5), September 2002, pp. 804–812. DOI: 10.2514/2.3000.

12. Ye, Z., Xu, G.-h., Shi, Y.-j., and Xia, R.-z., "A High-efficiency Trim Method for CFD Numerical Calculation of Helicopter Rotors," *International Journal of Aeronautical and Space Sciences*, Vol. 18, (2), June 2017, pp. 186–196. DOI: 10.5139/IJASS.2017.18.2.186.

13. Fu, J., and Vigevano, L., "An Efficient Helicopter Main Rotor Trim Method Based on Computational Fluid Dynamics," 49th European Rotorcraft Forum (ERF 2023), 2023.

14. Morino, L., "Helmholtz Decomposition Revisited: Vorticity Generation and Trailing Edge Condition," *Computational Mechanics*, Vol. 1, (1), March 1986, pp. 65–90. DOI: 10.1007/BF00298638.

15. Cottet, G.-H., and Koumoutsakos, P. D., *Vortex Methods: Theory and Practice*, Cambridge University Press, Cambridge ; New York, 2000.

16. Lindsay, K., and Krasny, R., "A Particle Method and Adaptive Treecode for Vortex Sheet Motion in Three-Dimensional Flow," *Journal of Computational Physics*, Vol. 172, (2), September 2001, pp. 879–907. DOI: 10.1006/jcph.2001.6862.

17. Brown, R. E., and Line, A. J., "Efficient High-Resolution Wake Modeling Using the Vorticity Transport Equation," *AIAA Journal*, Vol. 43, (7), July 2005, pp. 1434–1443. DOI: 10.2514/1.13679.

18. Tugnoli, M., Montagnani, D., Syal, M., Droandi, G., and Zanotti, A., "Mid-Fidelity Approach to Aerodynamic Simulations of Unconventional VTOL Aircraft Configurations," *Aerospace Science and Technology*, Vol. 115, August 2021, pp. 106804. DOI: 10.1016/j.ast.2021.106804.

19. Kim, J. W., and Lee, D. J., “Generalized Characteristic Boundary Conditions for Computational Aeroacoustics,” *AIAA Journal*, Vol. 38, (11), November 2000, pp. 2040–2049. DOI: 10.2514/2.891.

20. Splettstoesser, W. R., Schultz, K. J., Boxwell, D. A., and Schmitz, F. H., “Helicopter Model Rotor-Blade Vortex Interaction Impulsive Noise: Scalability and Parametric Variations,” Technical Report TM-84-A-7, Ames Research Center, Moffett Field, California, USA, December 1984.

21. Yu, Y. H., Tung, C., Gallman, J., Schultz, K. J., Van Der Wall, B., Spiegel, P., and Michea, B., “Aerodynamics and Acoustics of Rotor Blade-Vortex Interactions,” *Journal of Aircraft*, Vol. 32, (5), September 1995, pp. 970–977. DOI: 10.2514/3.46825.

22. PassMark, “[Dual CPU] AMD EPYC 7513 vs [Dual CPU] Intel Xeon Gold 6248 [Cpubenchmark.Net] by PassMark Software,” https://www.cpubenchmark.net/compare/4383.2vs3517.2/AMD-EPYC-7513-vs-Intel-Xeon-Gold-6248, April 2025.

23. Yu, Y. H., Tung, C., Field, M., Van Der Wall, B., Pausder, H.-J., Burley, C., Brooks, T., Beaumier, P., Delrieux, Y., Mercker, E., and Pengel, K., “The HART-II Test: Rotor Wakes and Aeroacoustics with Higher-Harmonic Pitch Control (HHC) Inputs - The Joint German/French/Dutch/US Project,” American Helicopter Society 58th Annual Forum, June 2002.

24. Renaud, T., Perez, G., Benoit, C., Jeanfaivre, G., and Péron, S., “Blade-Vortex Interaction Capture by CFD,” 34th European Rotorcraft, September 2008.

25. Schneider, O., “Comparison of Simple and Conditional Averaging Methodology Based on Results of the Hart II Wind Tunnel Test,” 1st International Forum on Rotorcraft Multidisciplinary Technology, 2007.

CLASSIFICATION & COPYRIGHT